

Study on Time-frequency Imaging of Ultrasonic Detection with Phase Shifted Fiber Bragg Grating Sensing

Lijun Meng^{1*}, Xin Tan², Quanquan Yu³

¹ State Key Laboratory of Precision Blasting, Jiangnan University, Delta Lake Road, No.8, 430056, Wuhan, China; Intelligent manufacturing College, Jiangnan University, Delta Lake Road, No.8, 430056, Wuhan, China, menglijun0408@163.com

² Intelligent manufacturing College, Jiangnan University, Delta Lake Road, No.8, 430056, Wuhan, China, tanpatrick@163.com

³ Intelligent manufacturing College, Jiangnan University, Delta Lake Road, No.8, 430056, Wuhan, China, 947112967@qq.com

Abstract: The influence of the wavelength difference between the laser source and the phase-shifted fiber Bragg grating (PS-FBG) on the intensity of the power demodulation system based on an adjustable laser source was studied experimentally, and the optimum of the output laser wavelength was determined. Then, the research on time-frequency imaging damage identification based on smooth pseudo-Wigner-Ville distribution was carried out. The Time of Flight of the acoustic wave signal was calculated and time compensation was made according to the Wigner-Ville distribution and the Lamb wave dispersion curve. The ultrasonic waves before and after damage were measured with spatially arranged PS-FBGs. The difference signals were processed in a window, and then the time-frequency energy of the normalized difference signal was imaged to assess the damage detection and location. Although the mode and group velocity of ultrasound measured by each fiber grating were different, the accurate location and identification of artificial damage in an aluminum alloy plate was realized by using only three PS-FBGs and a smooth Wigner time-frequency imaging method.

Keywords: Phase shifted fiber Bragg grating (PS-FBG), time-frequency analysis, ultrasonic detection, smooth pseudo-Wigner-Ville distribution, dispersion curve, damage imaging.

1. INTRODUCTION

Fiber Bragg Grating (FBG) has received extensive attention to replace the traditional electric ultrasonic transducer for ultrasonic wave measurement. Compared with the traditional piezoelectric ceramics, FBG can perform the high-sensitivity detection of broadband ultrasonic signals and has the characteristics of anti-interference ability, multi parameter distributed measurement, small size and light weight, and can effectively improve the reliability and efficiency of ultrasonic detection. Some researchers have used ultrasonic FBG sensors to detect cracks in aluminum alloy plates or defects such as delamination and deboning in carbon fiber reinforced plastics [1]-[5]. It has been found that the phase-shifted fiber Bragg grating (PS-FBG) has more advantages than FBG in the measurement of low strain wave with high-frequency because of its high wavelength selectivity and reflectivity and extremely narrow linewidth [6]. Wu et al. built an ultrasonic excitation and π PS-FBG sensing system and analyzed the spatial distribution sensitivity of π PS-FBG to ultrasonic waves [7]-[8]. Yu et al.

[9]-[10] used the acoustic emission signal amplitude ratios of the S_0 and A_0 modes and the peak frequency measured by the PS-FBG sensor to detect transverse cracks and delamination damage. Fink et al. used π PS-FBG to detect AE signals of lead breaking [11]. Liu et al. analyzed the influence of PS-FBG parameters on the sensitivity of ultrasonic wave measurement [12]. Guo et al. developed a PS-FBG wavelength tracking system for ultrasonic imaging of seismic physical mode [13]. There are also many researches on the PS-FBG high-frequency demodulation system for ultrasonic waves and acoustic emission measurements [14]-[18]. However, the current research is mainly focused on the theoretical research of the PS-FBG response characteristics to ultrasonic waves and the stable high-speed PS-FBG demodulation system. In the research, often only one fiber grating has been used to measure the ultrasonic signal. Due to the limited signal from a single fiber grating, it was often impossible to obtain the specific location of the damage. Although an increasing FBG arrangement can roughly locate the damage using FBG axial sensitivity to ultrasonic waves,

the spatial strain sensitivity difference and linear wavelength demodulation range between PS-FBG and FBG, as well as detection cost caused by increasing the number of gratings should be considered in the PS-FBG network arrangement. In addition, due to the limitations of current demodulation technology, the original signal measured by PS-FBG is often affected by temperature, quasi-static stress, etc., and there are still some problems in the extraction of effective signal features. Therefore, it is necessary to study the sensing characteristics of PS-FBG network and the wavelength demodulation range compared with FBG. The effective analysis and processing methods of the distributed PS-FBG signals and the damage identification strategy based on the distributed data also need to be carried out.

First, a distribution network of FBG and PS-FBG sensors for ultrasonic waves was designed. The response difference between PS-FBG and FBG to ultrasonic waves and PS-FBG best matching laser wavelength for signal demodulation system were studied experimentally. The experiment showed that PS-FBG has better ultrasonic induction intensity than FBG, but with a small wavelength demodulation range due to its narrow transmission spectrum. Therefore, careful wavelength matching between PS-FBG and the tunable laser should be performed. Then, how to obtain effective ultrasonic packet signals from the measured signals of the PS-FBG network was studied. The effective ultrasonic components from the PS-FBG network measurement signals were intercepted by a window function corresponding to the Lamb wave dispersion curve and the signal time-of-flight (TOF) calculated by the Wigner-Ville distribution time-frequency analysis method. Finally, the ultrasonic signals before and after damage were measured by spatially arranged PS-FBGs during the damage location experiment. The difference signals were time compensated and normalized based on the time delay theory, and then the time-frequency energy of the difference signal was imaged to identify the damage position according to the energy distribution. Experiments showed that the sensor network with only three PS-FBGs and the location method can well realize the damage identification and location in the $600\text{ mm} \times 600\text{ mm} \times 1\text{ mm}$ monitoring area of an aluminum alloy plate. The PS-FBG distributed layout structure, ultrasonic effective wave packet interception method and damage imaging strategy proposed in this paper provide a new idea for structural damage imaging and location using only several distributed PS-FBGs.

2. COMPARATIVE EXPERIMENT OF FBG AND PS-FBG RESPONSE TO ULTRASOUND

First, the response difference between PS-FBG and FBG to acoustic emission signals was studied. The experimental principle and device are shown in Fig. 1 and Fig. 2. The wavelength demodulation system based on an adjustable laser source (Yenista-TLS-AG-C) was used for both PS-FBG and FBG signal measurement. In the experiment, the output wavelength of the tunable laser was carefully set to intercept the single side slope of the FBG reflection spectrum or the PS-FBG narrow transmission spectrum. The change of the corresponding light intensity was measured by the photodetector with amplification gain (PAD-10CS-ES), and then the center wavelength changes of the corresponding

FBG or PS-FBG can be measured. PS-FBG and FBG were each pasted on the surface of a $600\text{ mm} \times 600\text{ mm} \times 1\text{ mm}$ aluminum alloy plate, and the layout positions of the acoustic emission excitation source, PS-FBGs and FBGs, are shown in Fig. 3 and Fig. 4. As shown in Fig. 3, the acoustic emission excitation point was at point A (red circle), where a $\Phi 200\text{ mm} \times 0.5\text{ mm}$ piezoelectric ceramic sheet was pasted. The voltage pulse signal generated by the signal generator (RIGOL-DG1022) was amplified by the voltage amplifier (PINTEK-HA-405) to excite the piezoelectric ceramic sheet and generate an acoustic emission signal in the plate. FBG and PS-FBG were arranged in parallel on the plate.

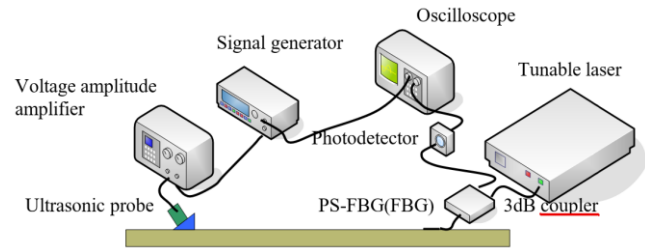


Fig. 1. Experimental principle of ultrasonic excitation PS-FBG/FBG sensing detection.



Fig. 2. Photo of the experimental device.

In a wavelength demodulation system with a tunable laser, the FBG length must be smaller than the ultrasonic wavelength to avoid the influence of the ultrasonic strain non-uniform micro-bending modulation on the FBG detection results [19]-[20]. The PS-FBG has a much smaller effective detection length than its own grating length due to the phase shift at its center and has an extremely sharp resonance for high sensitivity, and increasing the PS-FBG length can increase its ultrasonic detection sensitivity in a tunable laser-based demodulation system [21]. The lengths of the grating area of FBGs and PS-FBGs were 3 mm and 20 mm, respectively, and there was a phase shift of π in the center of the grating area of PS-FBG. Based on the estimation method of PS-FBG effective detection length [22], the effective grating length was represented by the full width at the half maxima of the PS-FBG power distribution curve. Its value was 4.6 mm, 3.8 mm, and 3.4 mm for the index modulation depths of $6e-4$, $7e-4$, and $8e-4$, respectively, as for the 20 mm PS-FBG. For the experiment, PS-FBG and FBG should be selected from the same manufacturer and batch, and their performance parameters must be approximately the same.

The ultrasonic wave used to excite the aluminum alloy plate had a frequency-thickness product of 0.1 MHz mm and 1 MHz mm, and the wavelengths of the main ultrasonic mode S0 were separately about 54 mm and 5.1 mm according to the dispersion characteristics of the Lamb wave and Fig. 15. The 3 mm FBG selected in the experiment can be used for the 0.1 MHz mm ultrasonic measurement because its grating length is far smaller than the ultrasonic wavelength, and the 20 mm PS-FBG can be used for the 0.1 MHz mm and 1 MHz mm ultrasonic measurement because its effective length is also smaller than the corresponding ultrasonic wavelength.

good signal strength, the laser output wavelength was set to the position around the half value bandwidth of the reflection spectrum and the middle slope position of the transmission narrow band for FBG and PS-FBG, respectively. The initial wavelengths of FBGs and PS-FBG and the corresponding tunable laser source setting wavelengths during demodulation are shown in Table 1.

Table 1. Parameters of each fiber grating.

Fiber grating	Initial center wavelength [nm]	Tunable laser setting wavelength [nm]
FBG1	1550.082	1550.432
FBG2	1549.945	1550.246
FBG3	1549.865	1550.166
FBG4	1549.941	1550.250
PS-FBG1	1549.836	1549.855
PS-FBG2	1549.956	1549.978
PS-FBG3	1549.930	1549.954

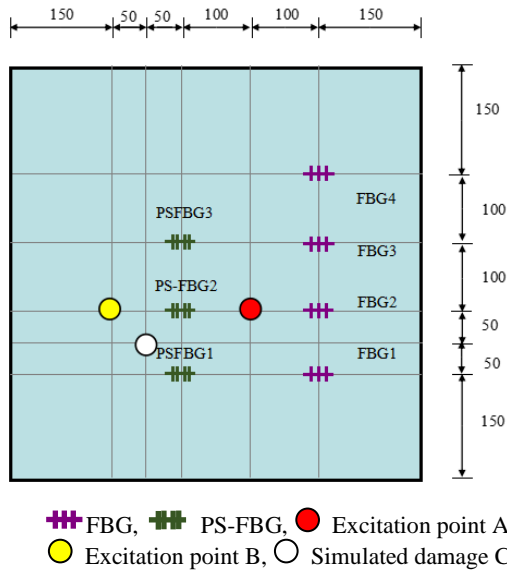


Fig. 3. Layout of FBGs and PS-FBGs.

At the same time, the signal generator produced a synchronous signal for the trigger of the oscilloscope during each measurement process to ensure the synchronization of each fiber grating between the measurement signal and the excitation signal. The measurement results of PS-FBG and FBG are shown in Fig. 5. From Fig. 5, it can be seen that each fiber grating measured the acoustic emission signal, with PS-FBG2 having the highest signal intensity. The FFT transformation of PS-FBG2 is shown in Fig. 6, and its main frequency was 93 kHz, which is essentially the same as the main frequency of the signal generator. The other signals also had similar dominant frequencies.

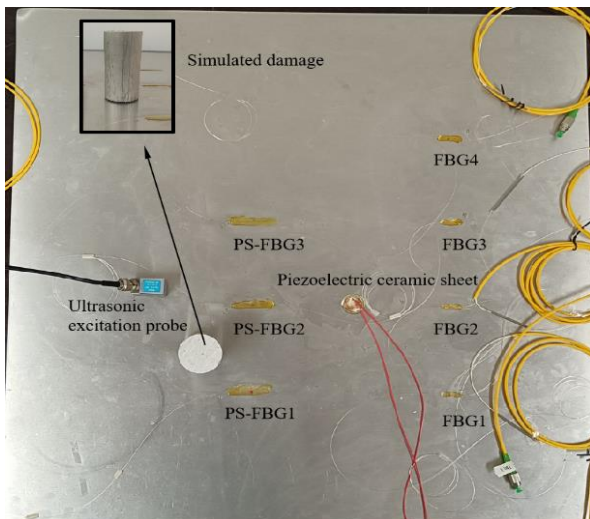


Fig. 4. Physical layout of PS-FBG/FBGs and excitation point.

The signal output from the signal generator was a 5-cycle sinusoidal signal with a frequency of 100 kHz and peak to peak value of 5 V. It was amplified about 80 times by the voltage amplifier to excite the piezoelectric ceramic sheet and generate an acoustic emission signal in the plate. The acoustic emission signals at the position of the pasted FBGs/PS-FBGs were obtained by the demodulation system in turn. To obtain

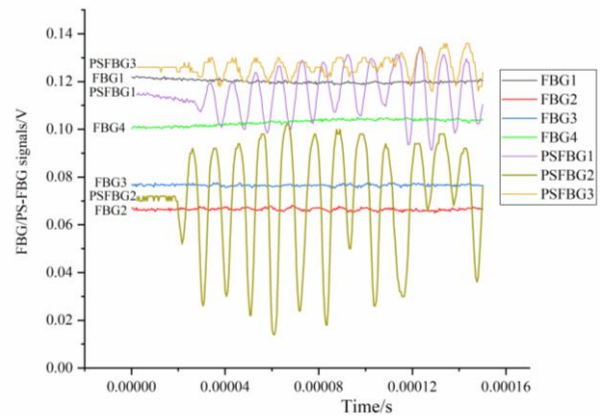


Fig. 5. Response signals of FBG and PS-FBG to the piezoelectric ceramic sheet.

According to Fig. 5, the peak-to-peak values of FBG and PS-FBG signals can be read in Fig. 7. It can be seen from Fig. 7 that the PS-FBG has a higher response intensity for the same acoustic emission source compared to FBG, and the closer FBG/PS-FBG was to the acoustic emission source, the stronger the ultrasonic signal was. Therefore, PS-FBG is more sensitive to ultrasonic signal measurement than FBG. The PS-FBG arranged along the axis of ultrasonic conduction had a higher signal strength. The closer to the ultrasonic source, the stronger was the signal from PS-FBG.

Then, the wavelength matching relationship between the adjustable laser source and PS-FBG was studied in the experiment. In the experiment, the demodulated signals of PS-FBG2 were measured under the same piezoelectric ceramic acoustic emission source by changing the output wavelength of the adjustable laser. Fig. 8 shows the response signals of PS-FBG2 under different wavelength differences (the difference between the central wavelength of laser source and the central wavelength of PS-FBG, and that was from 0.009 nm to 0.067 nm).

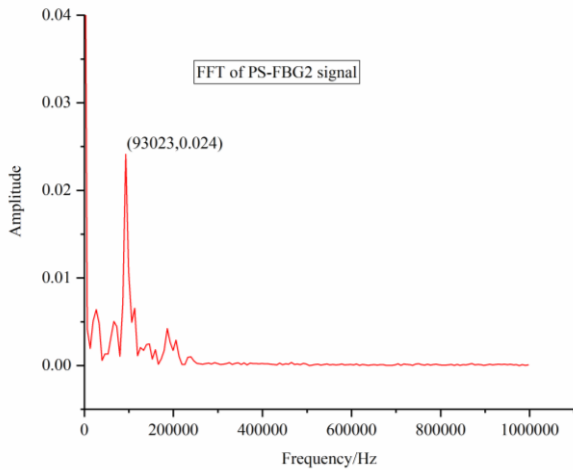


Fig. 6. FFT transformation of PS-FBG2 signal.

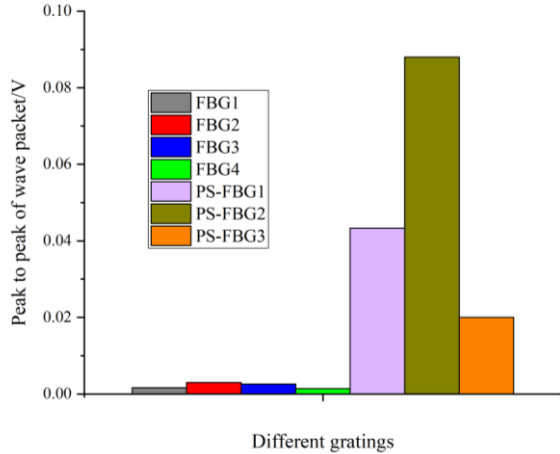


Fig. 7. Peak value and peak value of wave packet signal measured by different fiber gratings.

It can be seen from Fig. 8 that the signal strength detected by PS-FBG was different at different wavelength differences. According to Fig. 8, the variation of signal peak value was plotted with the wavelength difference in Fig. 9. As can be seen from Fig. 9, the detection signal intensity of PS-FBG showed two peaks with the increase of wavelength difference. As shown in Fig. 10, the spectral characteristics of the ideal PS-FBG are symmetrical with respect to its central wavelength. The one-sided spectrum of PS-FBG has a narrow-band transmission slope and a single-sided reflection spectrum slope, with the optimal values of laser wavelength on each slope. From Fig. 10, the maximum signal intensity

measured when the laser wavelength was set on the transmission narrow-band slope (Section AB) was much larger than that measured when set on the single-sided slope of the reflection spectrum (Section CD). As with PS-FBG2 in the experiment, the intensity of the acoustic emission signal was greatest when the wavelength difference was $\Delta\lambda = 0.017$ nm, and the demodulation system has the highest sensitivity.

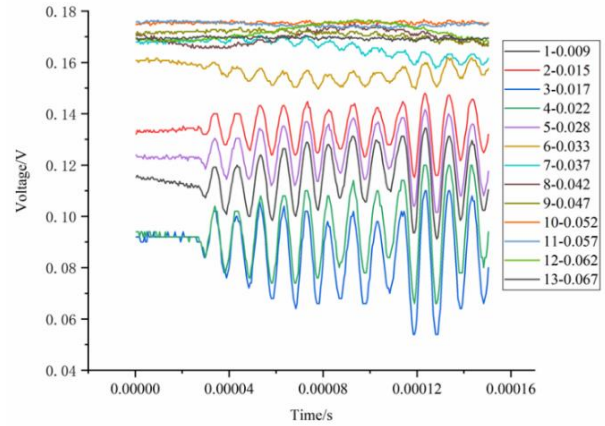


Fig. 8. Response of the same PS-FBG to acoustic emission signal at different laser wavelengths.

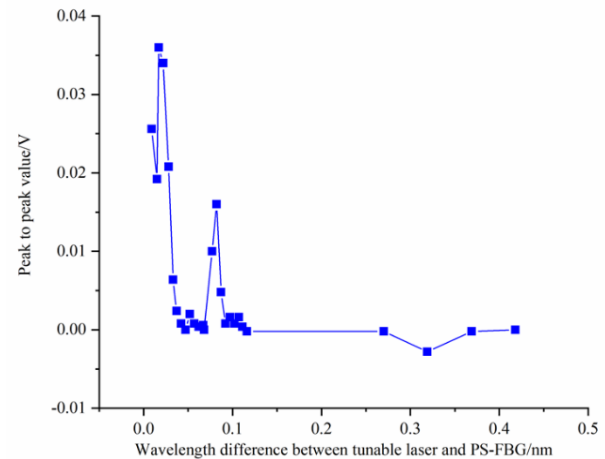


Fig. 9. Variation trend of response amplitude of PS-FB with laser wavelength.

3. EXPERIMENT ON DAMAGE DETECTION AND IMAGING

The experiment on damage imaging of PS-FBG and acoustic wave detection was conducted. The PS-FBGs shown in Fig. 3 and Fig. 4 were still used, and the demodulation method and experimental device were also the same as in the previous experiment. Due to the good directivity of the angle probe, it was used to excite the ultrasonic wave in the aluminum alloy plate in the experiment. The ultrasonic probe with $1 \text{ MHz} \times 30^\circ$ was placed at point B (yellow circle, as shown in Fig. 3 and Fig. 4) with a coupling device, and the ultrasonic transceiver acquisition card was used to excite the angle probe to generate ultrasonic waves. One of the multi-channel signals from the signal acquisition card was used as the trigger signal of the oscilloscope to ensure synchronization between the fiber grating measurement

signal and the excitation signal. A $\Phi 40 \text{ mm} \times 81 \text{ mm}$ aluminum column was placed at the position of point C (white circle, as shown in Fig. 3 and Fig. 4) to simulate the artificial damage of the plate surface. To ensure the effective contact between the aluminum column and the plate, a coin was placed between them.

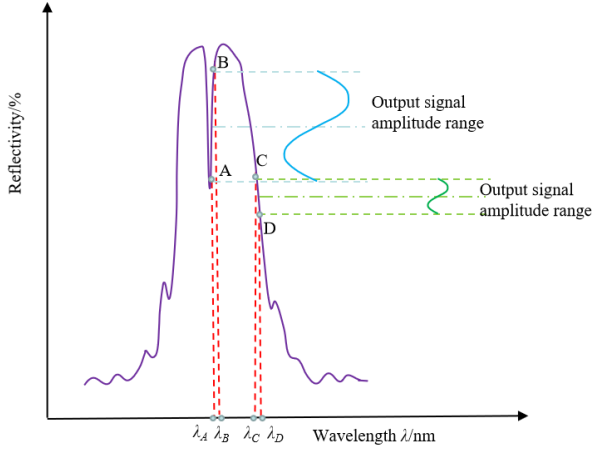


Fig. 10. Reflection spectrum of an ideal PS-FBG.

The key to structure damage localization and imaging is to determine the arrival time and TOF of the signals. Currently, the threshold method, correlation coefficient, Hilbert transform, and wavelet transform are mainly used to determine the arrival time of guided waves [23]-[25]. However, due to noise interference and approximate energy distribution, only a rough arrival time of the waves can be determined using these methods. In addition, the time-frequency analysis method is widely used in the analysis of the guided wave dispersion mode, the estimation of wave packet arrival time and the evaluation of the mechanical damage degree [26]-[27]. The Wigner-Ville Distribution (WVD) is a Fourier transform of the instantaneous correlation function of the signal and can accurately locate the time-frequency structure of the signal. The interference term can be removed by the time-frequency analysis of the smooth Wigner-Ville distribution (SPWV) method, and the SPWV of the signal $x(t)$ is as follows:

$$SPWV_x(t, \omega) = \iint g(u-t) h(\tau) x\left(t + \frac{\tau}{2}\right) x^*\left(t - \frac{\tau}{2}\right) e^{-j\omega\tau} dud\tau \quad (1)$$

where $g(t)$ is a time window function; $h(\tau)$ is a frequency window function.

SPWV method has more advantages in the evaluation of guided wave TOF compared with the Hilbert envelope and wavelet analysis [28]. Therefore, the SPWV is used to obtain the time-frequency characteristics and TOF of PS-FBG signals. According to the energy distribution of time-frequency analysis, we define the following function:

$$Q_u(t) = SPWV_u(t, \omega_c) \quad (2)$$

where ω_c refers to the angular frequency value corresponding to the maximum energy value in the SPWV of the signal $u(t)$.

$Q_u(t)$ reflects the time-domain energy distribution when the angular frequency is equal to ω_c . $Q_u(t)$ is the filtering energy of an extremely narrow passband around ω_c , which can eliminate the background noise interference and distinguish the main guided wave modes according to the energy distribution in time.

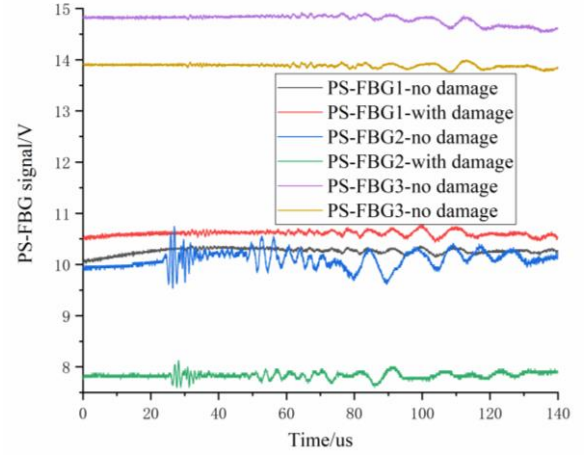


Fig. 11. PS-FBG raw signals.

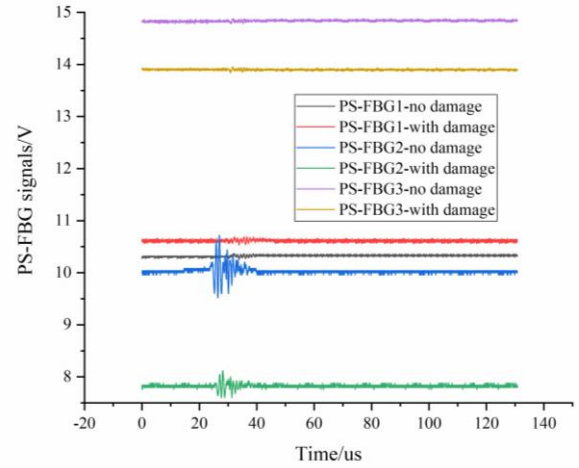


Fig. 12. PS-FBG signals after preliminary processing.

The ultrasonic wave excited by an ultrasonic probe at point B would reach the piezoelectric ceramic sheet at point A, and then low-frequency ultrasonic waves would be excited by the piezoelectric ceramic sheet due to the piezoelectric effect, which would be transmitted back to PS-FBG, resulting in the interference of the high-frequency ultrasound detected by PS-FBGs with the low-frequency ultrasound. The measurement signals from each PS-FBG before and after aluminum column loading were recorded respectively, as shown in Fig. 11. To remove the interference of the low-frequency piezoelectric ceramic signal, the time window was processed to intercept the high-frequency ultrasonic signal segment, and the quasi-DC component was used to supplement the signal in the measurement time. The processed signals are shown in Fig. 12. It can be seen from Fig. 12 that the signal intensity measured by the PS-FBGs varied with ultrasonic field positions and damage condition, and for the same fiber

grating, the signal amplitude with damage decreased to some extent compared to that without damage. The signal without damage measured by PS-FBG2 located on the acoustic axis was the strongest. To synchronously compensate for the probe delay and identify the guided wave mode, the signal from PS-FBG2 without damage was analyzed using SPWV and Wavelet Analysis. The PS-FBG2 original signal was normalized according to its signal amplitude and then transformed by the SPWV method, normalizing the energy according to the maximum value. The results are shown in Fig. 13. The signal of PS-FBG2 was processed by "cmor3-3" wavelet packet transform and the result was normalized by the maximum value of wavelet energy to obtain the time-frequency image, as shown in Fig. 14. From Fig. 13 and Fig. 14, it can be seen that the wave packet energy of PS-FBG2 is mainly concentrated in the time domain (20 μ s, 34 μ s) and frequency domain (0.5 MHz, 1.5 MHz). The energy peaks obtained by SPWV and wavelet analysis appeared at (0.82 MHz, 27.54 μ s) and (0.83 MHz, 27.26 μ s), respectively. The two analysis methods had similar time-frequency energy distributions, while the energy distribution noise interference of the SPWV method was lower, and the energy was more concentrated than in the Wavelet Analysis. Therefore, the time-frequency value at maximum energy obtained by the SPWV method was used for waveform time registration to eliminate the time delay and position error of the ultrasonic probe.

The ultrasonic wave is transmitted in the form of a Lamb wave in a thin plate. Ultrasonic waves are divided into symmetric modes and asymmetric modes. Each mode has a different order and different Lamb wave modes satisfy the following dispersion equation.

Symmetric modal dispersion equation:

$$\frac{\tan(qh)}{\tan(ph)} = -\frac{4k^2pq}{(q^2-k^2)^2} \quad (3)$$

Asymmetric modal dispersion equation:

$$\frac{\tan(qh)}{\tan(ph)} = -\frac{(q^2-k^2)^2}{4k^2pq} \quad (4)$$

in which

$$p^2 = \frac{\omega^2}{c_L^2} - k^2 \quad q^2 = \frac{\omega^2}{c_T^2} - k^2 \quad (5)$$

C_L and C_T are the velocity of the longitudinal wave and the transverse wave, respectively; H is half thickness of the plate, ω is the angular frequency of the ultrasonic wave, and k is the wave number. There is a relationship between the phase velocity C_p and the wavelength λ : $C_p = \omega\lambda/2\pi$. The parameters of the aluminum laminate used in the experiment are shown in Table 2. Using the table data and Formulas (3), (4) and (5), the calculated dispersion curve is shown in Fig. 15.

ω_{ci} and t_{ci} represent the angular frequency and arrival time corresponding to the maximum energy value in the SPWV signal of the i th PS-FBG without damage, respectively. From the dispersion curve shown in Fig. 14, the group velocity V_{cgi} and the ultrasonic mode of the ultrasonic wave with dominant

frequency ω_{ci} can be obtained. Assuming that the distance between the ultrasonic probe and the i th PS-FBG is L_i , the theoretical TOF of the dominant frequency ultrasonic wave is $t_{0i} = L_i/V_{cgi}$, and then the compensation time for the overall forward translation of the i th PS-FBG signal is $\Delta t_i = t_{0i} - t_{ci}$. Synchronous compensation was also performed for the measurement signal of the i th PS-FBG when there was artificial damage with the same compensation time Δt_i . For PS-FBG2, the arrival time and angular frequency of the main frequency corresponding to the maximum energy value were $t_{c2} = 27.54 \mu$ s and $\omega_{c2} = 0.82$ MHz, respectively. According to the dispersion curve, this ultrasonic wave corresponds to the S_0 mode, and the theoretical group velocity of the wave packet was $V_{cg2} = 5211.56$ m/s. The theoretical distance from the ultrasonic probe to PS-FBG2 was $L_2 = 100$ mm, therefore the theoretical time for the S_0 mode to reach PS-FBG2 was $t_{02} = 19.188 \mu$ s. The compensation time of the whole PS-FBG2 was $\Delta t_2 = t_{02} - t_{c2} = 8.352 \mu$ s.

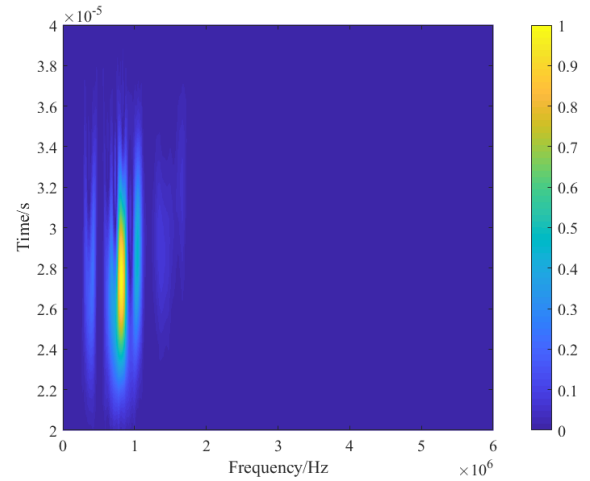


Fig. 13. SPWV of PS-FBG2 without damage.

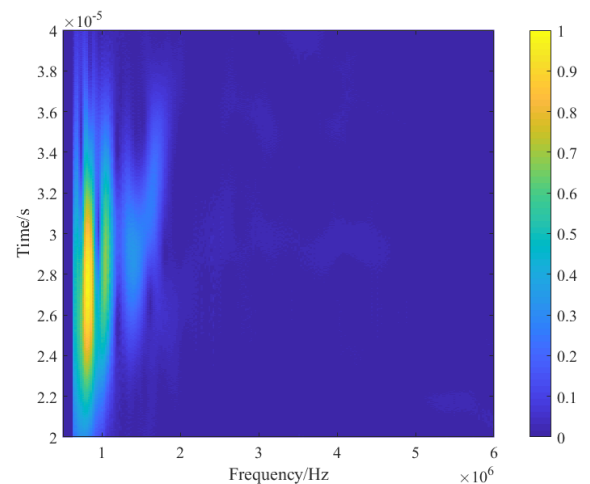


Fig. 14. Wavelet Analysis of PS-FBG2 without damage.

After time compensation, the signals before and after damage to PS-FBGs were subtracted and normalized on three paths to obtain the difference signal.

Table 2. Physical parameters of the aluminum alloy plate.

Parameter	Elastic Modulus [GPa]	Density [kg/m ³]	Poisson's ratio
Value	69.3	2680	0.33

The signal is normalized by the following formula:

$$\bar{u}_i(t) = \frac{u_i(t)}{\max(u_i(t))} \sqrt{\frac{d_i}{d}} \quad (6)$$

where $\bar{u}_i(t)$ is the signal measured by the i th PS-FBG, d_i is the distance from the ultrasonic source to the i th PS-FBG, and d is the distance from the ultrasonic source to the reference grating. In this paper, the second phase-shift grating PS-FBG2 was used as the reference grating.

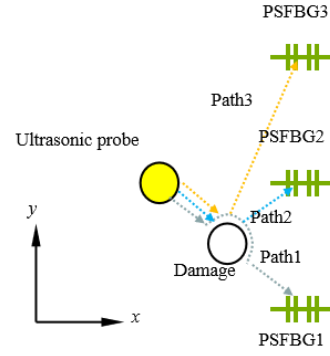
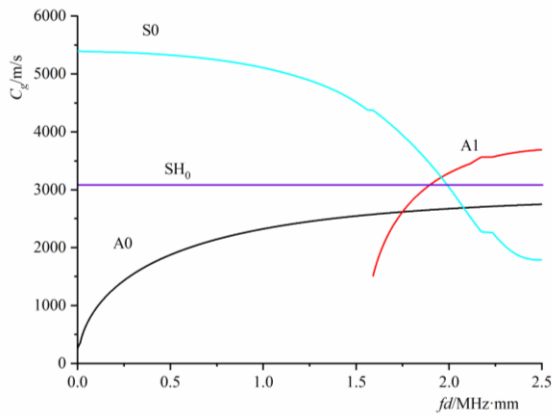
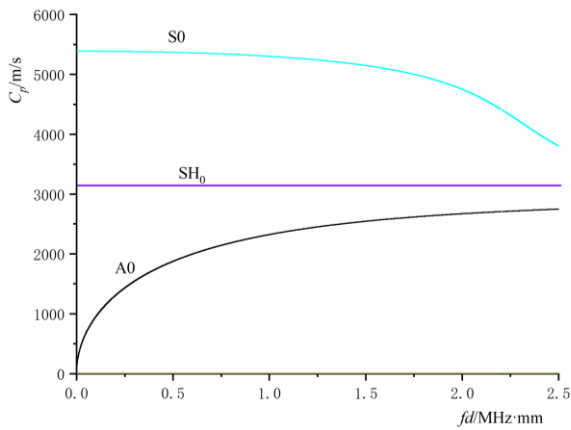


Fig. 16. Propagation path of the ultrasonic wave and imaging area.



(a) Group velocity curve



(b) Phase velocity curve

Fig. 15. Dispersion curve of the aluminum alloy plate.

As shown in Fig. 16, the ultrasonic wave would be scattered in the plate when it hits the damage. The position information of the damage can be obtained by analyzing the difference signals before and after the damage. The formula for the differential signal is:

$$u_i^{-diff}(t) = u_i^{-2}(t) - u_i^{-1}(t) \quad (7)$$

$u_i^{-1}(t)$ and $u_i^{-2}(t)$ are the signals measured by the i th PS-FBG if there was a defect and no defect, respectively.

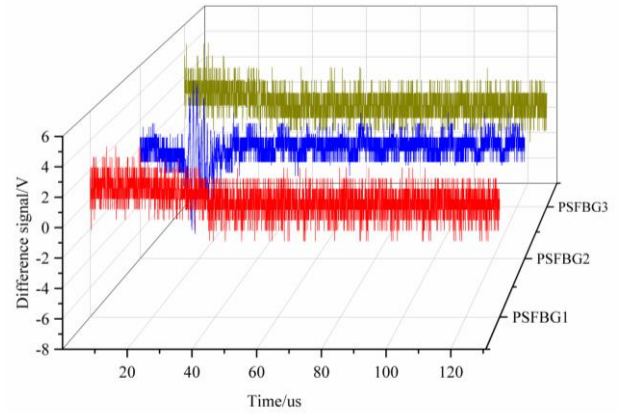


Fig. 17. Difference signal after normalization.

The difference signal after normalization is given in Fig. 17, and it can be used for spatial imaging of structural damage, in which the time-frequency energy at point (x, y) caused by the difference signal $u_i^{-diff}(t)$ can be expressed as:

$$I_i^{diff}(x, y) = Q_i^{diff} \left(\frac{d_{xy}}{c_{gi}} \right) \quad (8)$$

c_{gi} is the group velocity of ultrasonic wave with dominant frequency ω_{ci} , and (x, y) is the coordinate of any point in the plate, (x_0, y_0) is the coordinate of the ultrasonic excitation point, (x_i, y_i) is the coordinate of the i th PS-FBG. d_{xy} is the sum of the distances from the point (x, y) to the excitation point and the PS-FBG.

$$d_{xy} = \sqrt{(x_0 - x)^2 + (y_0 - y)^2} + \sqrt{(x_i - x)^2 + (y_i - y)^2} \quad (9)$$

By superimposing the time-frequency energy distribution of the difference signals measured by all PS-FBGs, the energy of all points on the plate can be calculated, and the energy of each point can be imaged to realize the damage identification.

$$I(x, y) = \sum I_i^{diff}(x, y) \quad (10)$$

The imaging calculation process followed the steps shown in Fig. 18, and the calculation results are shown in Fig. 19. In

Fig. 19, the symbol circle represents the position of the ultrasonic probe, the symbol "+" reflects the pasting position of PS-FBG, and the symbol "*" marks the actual position of the simulated defects. To better reflect the positional relationship between the imaging results and the actual artificial damage, only the positions with a time-frequency energy greater than 1500 are shown in Fig. 19(b). It can be seen from Fig. 19(b) that the two-dimensional imaging results are in good agreement with the actual position of the damage. Although the ultrasonic waves conducted in the plate had many different modes and group velocities, and static noise and boundary echo interference occurred, the damage of thin plate can be accurately located with three PS-FBGs using the SPWV time-frequency imaging method. When the number of PS-FBG is further increased, two-dimensional imaging can better reflect the size of the artificial damage.

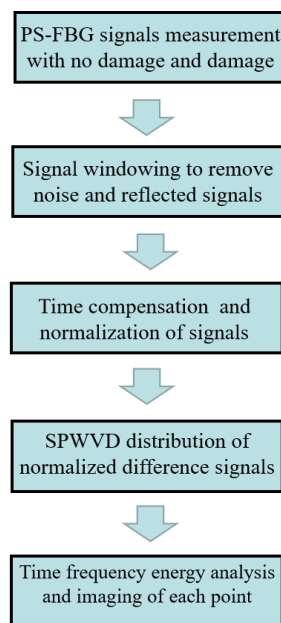


Fig. 18. Basic principles and steps of damage imaging.

4. CONCLUSION

This paper presents a time-frequency analysis algorithm for mechanical structure damage location imaging using ultrasonic signals measured by distributed PS-FBGs. Experimental results showed that PS-FBG has better ultrasonic sensitivity than FBG. The matching relationship between the adjustable laser wavelength and PS-FBG wavelength was studied experimentally, and the optimum laser wavelength for PS-FBG high-speed signal demodulation was determined. The Lamb wave arrival time was extracted by the SPWV transform method, and then the wave mode and velocity of the Lamb wave in the aluminum alloy plate were determined based on the dispersion curve. Finally, the ultrasonic signals in the aluminum alloy plate before and after damage were measured by PS-FBGs arranged in space, and the difference signals were normalized and compensated based on the time delay. The main frequency of the SPWV transform results of differential signals were two-dimensionally energy imaged, and the damage location was evaluated based on energy. This time-

frequency imaging method can effectively remove the interference of other low-frequency signals, and make full use of the sensor network composed of multiple PS-FBGs to realize the identification and location of mechanical structural damage. The method is simple and economical, and shows great potential for expanding the ultrasonic excitation – PS-FBG sensor technology in the field of structural damage location.

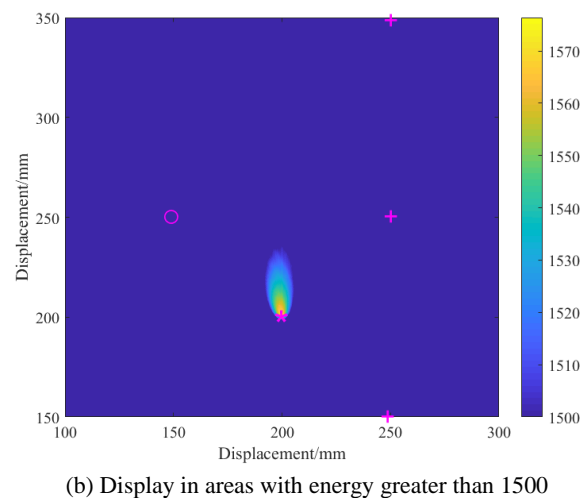
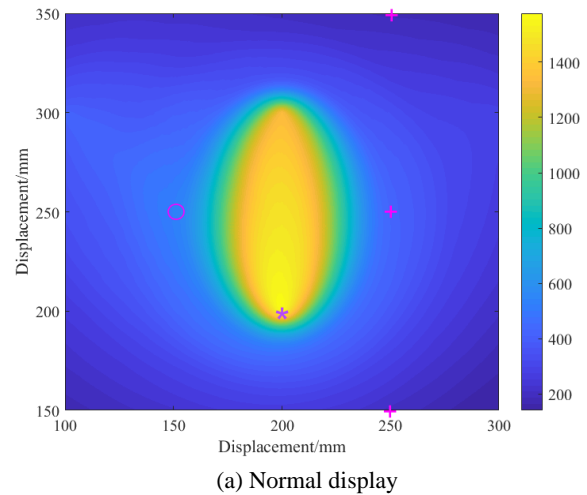


Fig. 19. Damage imaging diagram in plate (the circle represents the location and size of simulated damage).

ACKNOWLEDGMENT

This study was supported by the State Key Laboratory of Precision Blasting, Jiangnan University (No. PBSKL2022203), National Natural Science Foundation of China (No. 51505187), and Scientific Research Project of Jiangnan University (No. 2021yb151).

REFERENCES

- [1] Tsuda, H., Lee, J.R., Guan, Y., Takatsubo, J. (2007). Investigation of fatigue crack in stainless steel using a mobile fiber Bragg grating ultrasonic sensor. *Optical Fiber Technology*, 13 (3), 209-214. <https://doi.org/10.1016/j.yofte.2006.12.003>

- [2] Takeda, N., Okabe, Y., Kuwahara, J. (2005). Development of smart composite structures with small-diameter fiber Bragg grating sensors for damage detection: Quantitative evaluation of delamination length in CFRP laminates using lamb wave sensing. *Composites Science and Technology*, 65 (15-16), 2575-2587. <https://doi.org/10.1016/j.compscitech.2005.07.014>
- [3] Lam, P.M., Lau, K.T., Ling, H.Y., Su, Z., Tam, H.Y. (2009). Acousto-ultrasonic sensing for delaminated GFRP composites using an embedded FBG sensor. *Optics & Lasers in Engineering*, 47 (10), 1049-1055. <https://doi.org/10.1016/j.optlaseng.2009.01.010>
- [4] Frieden, J., Cugnoni, J., Botsis, J., Gmuer, T. (2012). Low energy impact damage monitoring of composites using dynamic strain signals from FBG sensors – part I: Impact detection and localization. *Composite Structures*, 94 (2), 438-445. <https://doi.org/10.1016/j.compstruct.2011.08.003>
- [5] Gomez, J., Jorge, I., Durana, G., Arrue, J., Zubia, J., Aranguren, G., Montero, A., Lopez, I. (2013). Proof of concept of impact detection in composites using fiber Bragg grating arrays. *Sensors*, 13 (9), 11998-12011. <https://doi.org/10.3390/s130911998>
- [6] Wu, Q., Okabe, Y. (2012). High-sensitivity ultrasonic phase-shifted fiber Bragg grating balanced sensing system. *Optics Express*, 20 (27), 28353-28362. <https://doi.org/10.1364/OE.20.028353>
- [7] Wu, Q., Okabe, Y., Saito, K., Yu, F. (2014). Sensitivity distribution properties of a phase-shifted fiber Bragg grating sensor to ultrasonic waves. *Sensors*, 14 (1), 1094-1105. <https://doi.org/10.3390/s140101094>
- [8] Wu, Q., Okabe, Y. (2014). Novel real time acousto ultrasonic sensors using two phase-shifted fiber Bragg gratings. *Journal of Intelligent Material Systems and Structures*, 25 (5), 640-646. <https://doi.org/10.1177/1045389X13483028>
- [9] Yu, F., Wu, Q., Okabe, Y., Kobayashi, S., Saito, K. (2016). The identification of damage types in carbon fiber reinforced plastic cross-ply laminates using a novel fiber-optic acoustic emission sensor. *Structural Health Monitoring*, 15 (1), 93-103. <https://doi.org/10.1177/1475921715624503>
- [10] Yu, F.M., Okabe, Y., Wu, Q., Shigeta, N. (2016). A novel method of identifying damage types in carbon fiber-reinforced plastic cross-ply laminates based on acoustic emission detection using a fiber-optic sensor. *Composites Science & Technology*, 135, 116-122. <https://doi.org/10.1016/j.compscitech.2016.09.017>
- [11] Fink, T., Qi, Z., Ahrens, W., Ming, H. (2012). Study of π -phase-shifted, Fiber Bragg gratings for ultrasonic detection. In *Fiber Optic Sensors and Applications IX*. SPIE Vol. 8370. <https://doi.org/10.1117/12.920810>
- [12] Rosenthal, A., Razansky, D., Ntziachristos, V. (2011). High-sensitivity compact ultrasonic detector based on a pi-phase-shifted fiber Bragg grating. *Optics Letters*, 36 (10), 1833-1835. <https://doi.org/10.1364/OL.36.001833>
- [13] Liu, T., Han, M. (2012). Analysis of π -phase-shifted fiber Bragg gratings for ultrasonic detection. *IEEE Sensors Journal*, 12 (7), 2368-2373. <https://doi.org/10.1109/JSEN.2012.2189383>
- [14] Guo, J., Xue, S., Zhao, Q., Yang, C. (2014). Ultrasonic imaging of seismic physical models using a phase-shifted fiber Bragg grating. *Optics Express*, 22 (16), 19573-19580. <https://doi.org/10.1364/OE.22.019573>
- [15] Zhang, F.Y., Jiang, M.S., Sui, Q.M., Lü, S.S., Jia, S. (2017). Acoustic emission localization technique based on fiber Bragg grating sensing network and signal feature reconstruction. *Acta Physica Sinica*, 66 (7), 074210. <https://doi.org/10.7498/aps.66.074210>
- [16] Sante, R.D., Bastianini, F. (2015). Temperature-compensated fibre Bragg grating -based sensor with variable sensitivity. *Optics & Lasers in Engineering*, 75, 5-9. <https://doi.org/10.1016/j.optlaseng.2015.06.002>
- [17] Zhu, Y., Hu, L., Liu, Z., Han, M. (2019). Ultrasensitive ultrasound detection using an intracavity phase-shifted fiber Bragg grating in a self-injection-locked diode laser. *Optics Letters*, 44 (22), 5525-5528. <https://doi.org/10.1364/OL.44.005525>
- [18] Xu, Y., Zhang, L., Gao, S., Lu, P., Mihailov, S., Bao, X. (2017). Highly sensitive fiber random grating-based random laser sensor for ultrasound detection. *Optics Letters*, 42 (7), 1353-1356. <https://doi.org/10.1364/OL.42.001353>
- [19] Lee, J.R., Tsuda, H., Toyama, N. (2007). Impact wave and damage detections using a strain-free fiber Bragg grating ultrasonic receiver. *NDT&E International*, 40 (1), 85-93. <https://doi.org/10.1016/j.ndteint.2006.07.001>
- [20] Dwivedi, K.M., Trivedi, G., Khijwania, S.K., Osuch, T. (2020). Design and numerical analysis of a highly sensitive ultrasonic acoustic sensor based on π -phase-shifted fiber Bragg grating and fiber Mach-zehnder interferometer interrogation. *Metrology and Measurement Systems (Metrologia i Systemy Pomiarowe)*, 27 (2), 289-300. <https://doi.org/10.24425/mms.2020.132775>
- [21] Liu, T., Han, M. (2012). Analysis of π -phase-shifted fiber Bragg gratings for ultrasonic detection. *IEEE Sensors Journal*, 12 (7), 2368-2373. <https://doi.org/10.1109/JSEN.2012.2189383>
- [22] Zhai, H.Z., Wu, Q., Xiong, K., Wang, R. (2019). π -phase-shifted fiber Bragg grating for strain measurement with high spatial resolution. *IEEE Photonics Technology Letters*, 31 (16), 1335-1338. <https://doi.org/10.1109/LPT.2019.2926849>
- [23] Jiao, J.P., Drinkwater, B.W., Neild, S.A., Wilcox, P.D. (2009). Low-frequency vibration modulation of guided waves to image nonlinear scatterers for structural health monitoring. *Smart Materials & Structures*, 18 (6), 065006. <https://doi.org/10.1088/0964-1726/18/6/065006>
- [24] Wang, X., Tse, P.W., Mechefske, C.K., Hua, M. (2010). Experimental investigation of reflection in guided wave-based inspection for characterization of pipeline defects. *NDT&E International*, 43 (4), 365-374. <https://doi.org/10.1016/J.NDTEINT.2010.01.002>

- [25] Zhu P., Yan H. (2022). Damage identification of flexible PVC substrate based on wavelet decomposition and limit learning machine. *Journal of Vibration and Shock*, 13, 220-227.
<https://doi.org/10.13465/j.cnki.jvs.2022.13.028>
- [26] Liu, X., Jiang, Z., Yan, Z. (2012). Improvement of accuracy in damage localization using frequency slice wavelet transform. *Shock and Vibration*, 19 (4), 585-596. <https://doi.org/10.3233/SAV-2011-0652>
- [27] Lemistre, M., Balageas, D. (2001). Structure health monitoring system based on diffracted Lamb wave analysis by multiresolution processing. *Smart Materials and Structures*, 10 (3), 504-511.
<https://doi.org/10.1088/0964-1726/10/3/312>
- [28] Tang, X., Li, Q. (2016). *Time Frequency Analysis and Wavelet Transform* (2nd Ed.). China Science Press, ISBN 9787030475428.

Received August 13, 2022

Accepted April 11, 2023